Enhancing and tuning phonon transport at vibrationally mismatched solid-solid interfaces

Timothy S. English,* John C. Duda, Justin L. Smoyer, Donald A. Jordan, and Pamela M. Norris†
Department of Mechanical and Aerospace Engineering, University of Virginia, Charlottesville, Virginia 22904, USA

Leonid V. Zhigilei‡
Department of Materials Science and Engineering, University of Virginia, Charlottesville, Virginia 22904, USA
(Received 19 August 2011; revised manuscript received 11 December 2011; published 23 January 2012)

The thermal conductance of interfaces plays a major role in defining the thermal properties of nanostructured materials in which heat transfer is predominantly phonon mediated. Ongoing research has improved the understanding of factors that govern interfacial phonon transport as well as the ability to predict thermal interface conductance. However, despite this progress, the ability to control interface conductance remains a major challenge. In this manuscript, we present a method to enhance and tune thermal interface conductance at vibrationally mismatched solid-solid interfaces. Enhancement is achieved through the insertion of an interfacial film with mediating vibrational properties, such that the vibrational mismatch at the interface is bridged, and consequently, the total interface conductance is enhanced. This phenomena is explored using nonequilibrium molecular dynamics simulations, where the effects of altering the interfacial film thickness, vibrational spectrum, and the temperature of the system are investigated. A systematic study of these pertinent design parameters explores the ability to enhance and tune phonon transport at both ideal (sharp) and nonideal (compositionally disordered) interfaces. Results show that interface conductance can be broadly enhanced by up to 53% in comparison to the vibrationally mismatched baseline interface. Additionally, we find that compositional disorder at an interface does not imply a deterministic change in interface conductance, but instead, that the influence of compositional disorder depends on the characteristics of the disordered region itself. These results, in contrast to macroscopic thermal transport theory, imply that it is possible to increase thermal conductance associated with interface scattering by adding more material along the direction of heat flux.

DOI: 10.1103/PhysRevB.85.035438 PACS number(s): 68.35.Ja, 63.22.−m, 68.60.Dv, 44.10.+i

I. INTRODUCTION

Solid-solid interfaces are ubiquitous features found in all micro and nanostructures. However, in the context of phonon-dominated thermal transport, an interface presents an added site for phonon scattering and impedes the propagation of thermal energy.[1] This scattering is quantified in terms of a thermal interface conductance (h_{BD}), which poses a number of challenges in managing thermal properties and dissipating excess thermal energy on the micro and nanoscale. Thermal interface conductance is defined as

$$h_{BD} = \frac{q}{\Delta T} = \frac{1}{R_{BD}}, \tag{1}$$

where q is the applied heat flux, ΔT is the temperature drop due to the presence of an interface, and R_{BD} is an equivalent thermal resistance. The fact that h_{BD} has become the limiting thermal conductance (dominant thermal resistance) in a wide range of nanostructures has been extensively documented in the literature.[2]

Interface conductance has been the subject of numerous studies with the objectives of better understanding and predicting interfacial thermal transport when phonons are the dominant energy carriers.[2] A major motivation for studying h_{BD} stems from its governing role in determining both thermophysical and interdependent functional properties (i.e., electrical, optical, magnetic) in technologically relevant nanostructures. For example, h_{BD} impacts the properties of superlattice structures,[3–5] including those used in semiconductor lasers,[6,7] light emitting diodes (LEDs),[8] and other optoelectronics.[9,10] A growing body of literature has also identified h_{BD} as a critical factor in the design of thermal interface materials,[11] thermoelectrics,[12] phase change memory,[13,14] superconducting thin films,[15] and various nanoelectronic cooling applications.[16] However, despite progress in understanding and predicting interfacial phonon thermal transport, the ability to control (greatly enhance and/or tune) h_{BD} remains a major challenge.[17]

To address this challenge, we present a method by which interfacial phonon thermal transport may be enhanced and tuned using a vibrational bridge. Specifically, we investigate an interfacial film, inserted into the interface, with mediating vibrational properties. Our findings indicate that selective design of the interfacial film to function as a vibrational bridge can reduce the effective ΔT across an interface structure, and therefore enhance h_{BD}. In this manuscript, we present the results of a systematic and comprehensive parametric study, performed using nonequilibrium molecular dynamics (NEMD) simulations. Furthermore, we investigate the phenomenon of enhancement of h_{BD} at both ideal (sharp) and nonideal (compositionally disordered) interfaces.

The remainder of this paper is organized as follows. Section II describes the method for enhancing h_{BD} and the interfacial film properties evaluated in the parametric study. Section III presents the details of the NEMD approach. In order to isolate the effects of vibrational mismatch and interface microstructure, we first investigate the enhancement of h_{BD} at ideal (sharp) interfaces, and results are reported in Sec. IV. The parametric study is revisited in Sec. V along with consideration of nonideal interface structures, characterized by compositional disorder. In Sec. VI, we provide concluding remarks and discuss the implications of the achieved enhancement of h_{BD} in the context of interfacial thermal transport theory.

II. ENHANCEMENT METHODOLOGY

A. Baseline interface structure

Throughout this study, all model materials have the face-centred cubic (fcc) structure. Vibrational properties of the modeled materials are controlled by altering the atomic mass, where the mass ratio $R_{x,y}$ between two materials comprising an interface is defined as

$$R_{x,y} = \frac{m_y}{m_x}. \tag{2}$$

This technique has been frequently used in molecular dynamics (MD) studies of phonon thermal transport.[18–23] Furthermore, it has been shown that the impact of cross-species interactions are more strongly governed by mass differences than by differences in bonding.[24] A baseline interface is constructed between two materials, A and B, which have an atomic mass of 40 and 120 atomic mass units (amu), respectively, and thus $R = 3$. This mass ratio is representative of several technologically relevant materials, including Si/Ge (2.6) and diamond/Si (2.3).

As a result of the A:B mass mismatch, the maximum phonon frequency (cutoff frequency) and distribution of phonon modes in materials A and B differ greatly. Figure 1 shows the phonon density of states (DOS) and dispersion in the direction perpendicular to the interface calculated via harmonic lattice dynamics[25] using the interatomic potential and parameters implemented in all NEMD simulations (see Sec. III). The difference in cutoff frequencies limits elastic (frequency conserving) scattering channels across the interface. In order for the energy associated with phonons whose frequencies are greater than $\omega_{\mathrm{B,cut}}$ (the maximum phonon frequency in material B) to traverse the interface, the phonons must scatter inelastically. As a result, with increasing vibrational mismatch, h_{BD} is expected to decrease.[26,27]

B. Interfacial film properties

The vibrationally mismatched and sharp A:B interface serves as the baseline interface. The proposed method for enhancing h_{BD} seeks to bridge the vibrational mismatch at the A:B interface via an interfacial film (material C) with mediating vibrational properties (see Fig. 2). We hypothesize

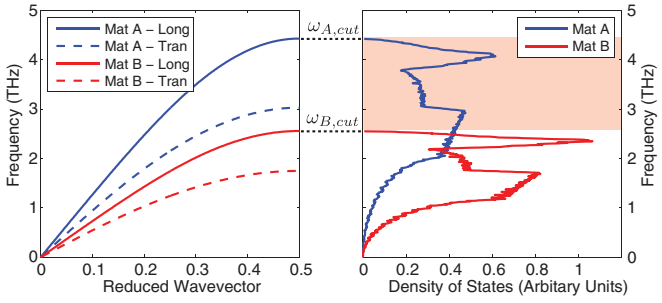

FIG. 1. (Color online) Phonon dispersion in the [100] direction and DOS of materials A and B calculated using harmonic lattice dynamics. The difference in cutoff frequencies is shown with respect to both the dispersion relationship and DOS. The red region demonstrates the vibrational mismatch and shows the density of phonon states in material A that do not exist in material B.

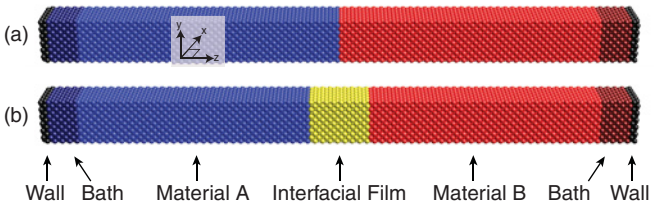

FIG. 2. (Color online) Schematic of computational domains representing (a) the baseline interface and (b) the enhanced interface structures with an 8-UC-thick interfacial film.

that the overall temperature drop across the entire interfacial region, now including a sandwiched film of material C, may be decreased, resulting in an effective increase in h_{BD}. This hypothesis may appear counterintuitive on several points. Most notably, the temperature drop across a lengthier interface structure under an applied heat flux would traditionally be expected to increase, reflecting an increase in the total thermal resistance of the structure. Moreover, the insertion of additional interfaces typically causes an increase in thermal resistance.[3,28] However, results in this study indicate that the added temperature drop due to diffusive thermal transport through the additional interfacial film material can be more than offset by the reduction in the temperature drop across the two newly formed interfaces.

Thermal transport properties of the interfacial film are expected to vary between two limits. In the limit as the interfacial film thickness approaches zero, the film is strongly influenced by confinement and interactions with the adjacent materials. As the interfacial film thickness increases, the enhancing interface structure transitions to that containing two independent interfaces, one between material A and C, and another between C and B, separated by an extended region of diffusive thermal transport through material C. In between these limits, there exists a number of complex interactions governing phonon thermal transport and scattering, where the wave nature of phonon transport is important due to the confined nature of the interfacial film and proximity of the two newly formed interfaces. With increasing film thickness, the combined conductance due to diffusive thermal transport through the interfacial film, in addition to the conductance at the two interfaces, is expected to fall below that of the baseline interface. As a result, the phonon mean-free path (MFP) and thermal conductivity (k) of the interfacial film composed of material C are expected to strongly influence the critical thickness at which the interfacial film no longer enhances, but in fact reduces, h_{BD}.

C. Parametric study

We perform a systematic study of the dependence of h_{BD} on the thickness and vibrational spectrum (via the mass) of the interfacial film. Initially, h_{BD} is determined for the baseline interface between materials A and B. Subsequently, an interfacial film (material C) is inserted between the materials comprising the baseline interface and varied in thickness from 2 conventional unit cells (UC) to 16 in 2 UC increments. For each of the eight values of thickness, the vibrational properties of the interfacial film are systematically varied by changing

the mass of atoms in the film between the values of 40 and 120 amu (the mass of atoms A and B) in 10 amu increments.

In addition to the simultaneous variation of these two factors, we also repeat the study at 10% and 50% of the crystal melting temperature (T_m). This upper limit is expected to bound the temperature range wherein the maximum enhancement of h_{BD} can be realized based on preliminary simulations and the following reasoning. Above 0.5 T_m, the thermal conductivities of material A and B are sufficiently low to ensure that the A:B interface is no longer the dominant factor limiting conductance of the sample structure considered in this work.

III. COMPUTATIONAL SETUP IN MD SIMULATIONS

The Lennard-Jones (LJ) potential is used to describe all interatomic interactions. While it cannot provide an adequate quantitative description of real materials except for systems composed of nonpolar molecules or noble gas atoms, the LJ potential is both computationally inexpensive and captures the general essence of anharmonic effects that govern scattering and thermal properties in the classical regime. As a result, many simulations have turned to this potential when investigating general effects in phonon thermal transport, rather than trying to recreate a specific material system.[20–22,29–35]

The LJ potential with a cutoff distance of 2.5σ is defined as

$$\Phi(r_{ij}) = \begin{cases} 4\epsilon\left[\left(\frac{\sigma}{r_{ij}}\right)^{12} - \left(\frac{\sigma}{r_{ij}}\right)^{6}\right], & r_{ij} < 2.5\sigma, \\ 0, & r_{ij} \geqslant 2.5\sigma, \end{cases} \quad (3)$$

where σ is the distance at which potential energy is zero, ϵ is the depth of the potential well, which is related to the strength of bonding, and r_{ij} is the separation between atoms i and j. The potential parameters used in this study are $\sigma = 3.37$Å and $\epsilon = 0.0503$ eV. A cutoff distance of 2.5σ was used in all simulations, beyond which atomic interactions are ignored.[36] A time step of 2 femtoseconds was used in all MD simulations, which was sufficient to ensure energy conservation in all simulations.

In the subsequent discussion, temperature and thermal conductivity values are presented in reduced LJ units defined as shown in Table I with a reference mass m of 40 amu. Below, the asterisk will be dropped, and each of these quantities will be presented in reduced units unless otherwise stated. As a point of reference, the melting temperature of the LJ materials in this study correspond to a reduced temperature of ~0.5.[21] Therefore the two temperatures explored in this study, 0.1 and 0.5 T_m, correspond to reduced temperatures of about 0.05 and 0.25, respectively. Similarly, h_{BD} is presented in a normalized form with respect to the baseline h_{BD} value at either 0.1 or 0.5 T_m. The absolute values of h_{BD} in this study are not immediately transferable to any real material system.

TABLE I. Nondimensionalization equations.

Temperature	$T^* = T\frac{k_B}{\epsilon}$
Thermal conductivity	$k^* = k\sqrt{\frac{m}{\epsilon}}\frac{\sigma^2}{k_B}$

Instead, normalization provides a self-consistent framework to examine the relative change in h_{BD} throughout the parametric study.

A. Computational domains

In all simulations, the computational domains contain 11,520 atoms and are $6 \times 6 \times 80$ UC in the x, y, and z dimensions (31.62 Å × 31.62 Å × 421.6 Å, pre-equilibration). To investigate the hypothesis outlined in Sec. II B, two crystals (A and B) are joined to form an interface with a square cross section (dimensions along the x and y axes) oriented such that the [100] crystallographic direction is extended along the z axis. The resulting interface serves as the baseline interface and is shown in Fig. 2(a).

An interfacial film is then inserted whose atomic mass and thickness are systematically varied. The length of material A and B in the z direction is reduced in equal amounts as the thickness of the interfacial film increases. In this manner, the total length of the computational domains along the z axis remains fixed at 80 UCs for all simulations in this study. An example of an enhanced interface structure is shown in Fig. 2(b). In each computational domain, the dark red atoms indicate the hot bath and the dark blue atoms indicate the cold bath, through which energy is added and removed from the computational domain, respectively. The black atoms serve as a rigid-wall boundary. The 80 UC dimension along the z axis adds considerably to the computation costs of the parametric study and is comparatively large for the study of h_{BD} via LJ crystals. However, this domain length is chosen to ensure that even at the maximum interfacial film thickness (16 UC), the remaining portions of material A and B along the z axis (27 UC each) are still generously outside the regime wherein size effects and the presence of baths would influence measured h_{BD} values. Size effects are discussed further in Sec. III C.

B. Nonequilibrium configuration

Initially, the system was equilibrated at a predefined temperature via a velocity scaling routine (either 0.1 or 0.5 T_m) and zero pressure maintained by a Berendsen barostat.[37] During the initial equilibration and subsequent NEMD simulations, periodic boundary conditions were applied in the x and y dimensions. Once equilibration was complete, an NEMD routine was implemented in order to establish a temperature gradient within the system. The addition of energy to (or removal from) the baths at either end of the computational domain was performed in a similar fashion to the procedure outlined in Ref. 38 for energy exchange between electronic and lattice systems in simulations of short pulse laser heating of metals. This routine slightly alters the forces acting on an atom, depending on the amount of energy to be added or removed. The total force acting on atom i is given by

$$F_{i,\text{total}} = F_i + \xi m_i v_i^T, \quad (4)$$

where m_i is the mass of the atom, v_i^T is the thermal velocity of the atom, and ξ is a scaling factor. This scaling factor is expressed as

$$\xi = q\frac{1}{2K^T} = \frac{\Delta E}{2\Delta t K^T}, \quad (5)$$

where Δt is the time step used in the MD integration of the equations of motion, ΔE is the amount of energy to be added to or removed from the bath per time step, and K^T is the total thermal kinetic energy of the bath. A constant thermal flux of 0.285 GWm^{-2} was added to the hot bath and removed from the cold bath at every time step during NEMD simulation. To ensure the bath regions were not perturbed far from equilibrium, they were sized such that the energy added to or removed from the baths in one time step was less than 1% of the bath kinetic energy. In all simulations, 8 monolayers per bath were sufficient to satisfy this constraint. This constant-energy approach was preferred over maintaining the baths at constant temperatures because the applied heat flux was exactly known and not subject to fluctuations. Simulations ran for 6 million time steps for a total simulation time of 12 nanoseconds.

During nonequilibrium heating, the system was divided into 80 equally sized slices along the z axis in order to calculate a spatial temperature profile. The temperature of each of these slices was determined using the relationship

$$\frac{3}{2}N_P k_B T_P = \sum_{i=1}^{N_P} \frac{1}{2} m_i \left(v_i^T\right)^2, \tag{6}$$

where N_P is the number of atoms in a particular slice P, and k_B is Boltzmann's constant. Each slice contained 144 atoms. Linear least-squares fits (LLSFs) of selected temperature slices versus simulation time were made for discrete time intervals during the simulation. The slopes of these LLSFs were used to monitor the establishment of a steady-state regime, as indicated by convergence of the slope to values oscillating around zero.

Once in a steady-state regime, the time-averaged temperature of each slice was calculated and a LLSF was applied to calculate the spatial temperature gradient in each material. In theory, researchers calculate h_{BD} using Eq. (1) by evaluating ΔT at the interface from the difference of the LLSFs in each material. In practice, however, a variety of techniques have been adopted in choosing the regions included in the LLSF and the offset from the interface over which ΔT is defined. The first few slices near baths and interfaces are frequently ignored due to nonlinear behavior in these regions. As a result, the absolute values of ΔT and thus h_{BD} are not generally comparable between NEMD studies. In this study, we make an effort to define ΔT in a self-consistent manner, where the slices to be ignored in the LLSF are determined by considering the spatial temperature gradient (thermal conductivity) given by each LLSF with respect to known bulk thermal conductivities calculated from an independent set of simulations. This simultaneously enforces two best practices. First, the leads of material A and B in the z direction are long enough to return bulk thermal conductivity values, such that size effects are negligible, and second, the temperature gradient is linear (i.e., a reasonable flux is chosen and Fourier's law is applicable).

This approach is outlined in Figs. 3(a) and 3(b), where the same offset from the interface, shown by the hatched regions, was considered across the parametric study for varying interfacial film thicknesses to ensure that ΔT was evaluated in a self-consistent manner. Figure 3(c) shows the bulk thermal conductivities of materials A and B at ten temperatures ranging from 0.06 to 0.5 T_m calculated via additional NEMD

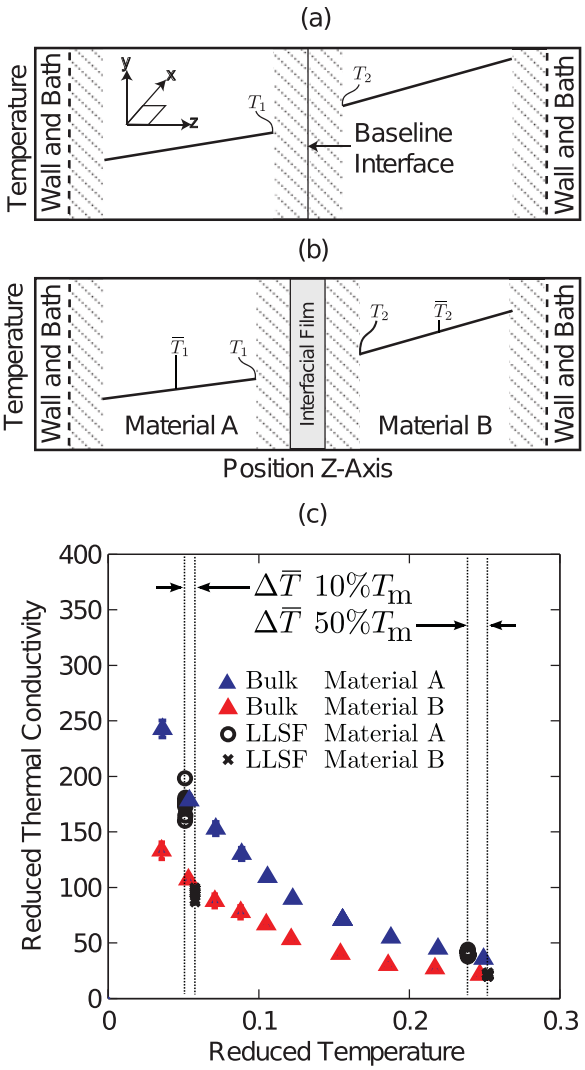

FIG. 3. (Color online) Schematics of the computational domain and geometric definition of $\Delta T = T_2 - T_1$ at (a) baseline and (b) enhanced interface structures. The hatched regions are excluded from the LLSFs to ensure that nonlinear effects near the interface and baths are not considered in the LLSFs. (c) Thermal conductivity is plotted vs reduced temperature from 6% to 50% of T_m. The thermal conductivities from a subset of the LLSFs used to determine h_{BD} throughout the study are compared to the bulk thermal conductivities predicted from additional MD simulations. The average temperatures over which the LLSFs are fit in each material are shown to provide a measure of the temperature drop, $\Delta(\overline{T}) = (\overline{T_2}) - (\overline{T_1})$, over the computational domain.

simulations where the computational domain ($6 \times 6 \times 80$ UC) is composed entirely of material A or B. Each bulk thermal conductivity value in Fig. 3(c) was calculated from a set of five independent simulations, and error bars represent $\pm$ one standard deviation (std). The thermal conductivities exhibit an approximately T^{-1} trend characteristic of Umklapp phonon-phonon scattering. The thermal conductivity values deduced from the slopes of the LLSF obtained in some of the calculations of h_{BD} are also plotted and agree well with the bulk values of thermal conductivity. From the LLSF of the spatial temperature gradient, an effective temperature drop across

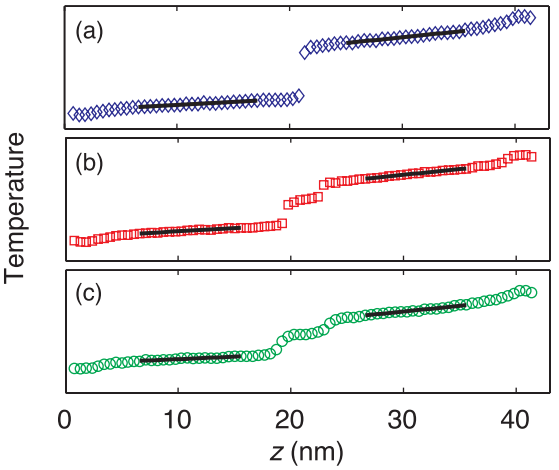

FIG. 4. (Color online) Raw temperature profiles at 0.1 T_m, (a) baseline interface, (b) sharp, 6 UC thick interfacial film with atomic mass of 80 amu, and (c) medium disorder, 6 UC thick interfacial film with atomic mass of 80 amu. Solid black lines show the LLSF in each material.

the entire interface structure was determined and interface conductance was calculated using Eq. (1).

Three raw temperature profiles drawn from the 0.1 T_m study are shown in Fig. 4, including (a) the baseline interface, (b) an enhanced, sharp, interface, and (c) an enhanced, compositionally disordered, interface. Solid black lines show the LLSF in each material. Note that the fits in (b) and (c) are each offset 3 additional UCs from the middle of the computational domain to account for the added 6 UC interfacial film. Therefore the temperature drop across the inner edge of each LLSF in (b) and (c) extends over a lengthier distance including the material forming the interfacial film. Compositional disorder causes a more gradual temperature drop near the interface, as compared to the abrupt temperature drops seen at the sharp interfaces in (a) and (b).

C. Finite size effects

If the dimensions of the computational domains are too small, confinement can significantly alter the phonon properties of the system and any trends assessed from MD simulations.[39] As a result, size effects were investigated by two methods at 0.1 T_m where any size effects should be most pronounced due to longer phonon MFPs. First, several domain sizes were investigated to confirm that pertinent phonon properties are independent of the system size. The results are shown in Fig. 5, which plots h_{BD} from five independent simulations of (a) varying domain lengths and (b) cross section widths. Baseline interface simulations down to 40 UC in length along the z axis repeatedly produced h_{BD} values, which fell within the uncertainty of those determined from the 80 UC domain, as shown in Fig. 5. Similar tests of varying cross sections at 0.1 T_m (80 UC along z axis) demonstrated that the 6×6 UC domains were sufficient to ensure size-independent results. The 4×4 domain showed significant nonlinear deviations in the thermal conductivity near the baths, while the 2×2 domains are clearly impacted by size effects.

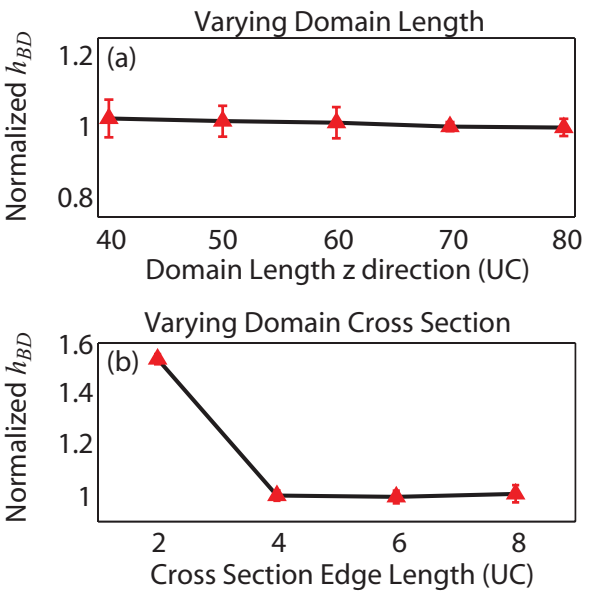

FIG. 5. (Color online) Normalized h_{BD} as a function of varying domain length (a) and width (b).

Second, the occupied phonon DOS were calculated and are shown in Fig. 6 for the x, y, and z directions at both 0.1 and 0.5 T_m for material B, as it contains more low-frequency, long-wavelength modes. The DOS is measured from a homogenous domain of material B, which is $6 \times 6 \times 80$ UC. In principle, the phonon DOS is calculated by taking the Fourier transform of the velocity autocorrelation function of an ensemble of atoms located in each crystal. In practice, however, the DOS is commonly estimated from the power spectral density. In order to calculate the power spectral density, the velocities of 100 atoms of the same material are stored during each time step of the simulation to provide a time series which spans 36,864 time steps. The power spectral density is then computed using a Welch function with eight 50% overlapping time series each containing 8,192 points.[40] After multiplying each time series by a corresponding Hamming window, the

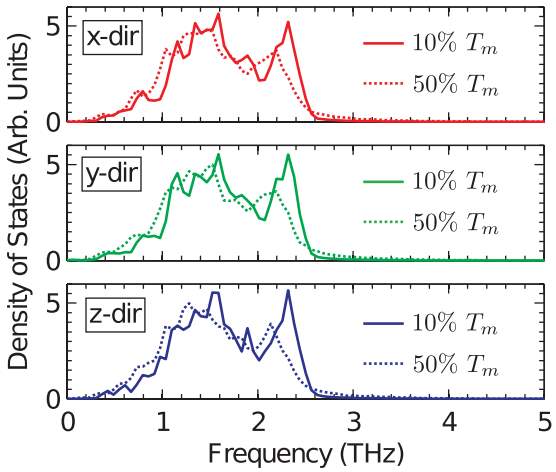

FIG. 6. (Color online) Plots of occupied DOS calculated for material B for each principal direction of the sample at 0.1 T_m and 0.5 T_m. The isotropic nature of the DOS in each direction indicates that phonon modes are not suppressed due to size effects.

fast Fourier transform is computed and the times series are ensemble averaged to provide the final estimation of a signal proportional to the occupied phonon DOS.

In Fig. 6, the phonon DOS in each of the three directions are indistinguishable. Throughout the parametric study, the computational domains are only 6 UC in the x and y dimensions, while the A and B crystals are considerably longer (27 UC in the shortest case in this study). The lack of distinct features in the DOS between the three directions indicates that 6 UC dimensions are large enough to produce the bulk phonon properties, which contribute substantially to thermal transport at these temperatures. Additionally, the cutoff frequencies of both materials agree with those predicted by harmonic lattice dynamics presented in Fig. 1. At higher temperatures, there is also a distinct broadening of the DOS associated with anharmonic effects, which dampen the phonon modes and cause a shift to lower frequencies.[41]

IV. ENHANCEMENT AT SHARP INTERFACES

The results of the parametric study at 0.1 and 0.5 T_{m} are shown in Figs. 7(a) and 7(b), respectively. The contour plots are constructed by interpolation of a grid of data points obtained in simulations performed with different values of interfacial film thickness and atomic mass. To assess the repeatability of the results, five independent simulations were performed for each parametric combination in the study. The resulting mean and standard deviation values are tabulated in Tables III and IV in the Appendix for the 0.1 and 0.5 T_{m} studies, respectively.

A. Low temperature (10% of melting temperature)

In the lower-temperature study, the boundary cases of 40-amu and 120-amu interfacial films at each thickness are closely related to the baseline interface. In these cases, the interfacial film is composed of entirely material A or B. These boundary cases were included to serve as a connection between the enhanced and baseline interface structures. They return nearly the baseline h_{BD} value (1.0) providing added validity to the sharp jump in h_{BD} exhibited between the 40 and 50 amu as well as the 110 and 120 amu cases. The departure from $h_{\mathrm{BD}} = 1.0$ with increasing interfacial film thickness at mass values of 40 and 120 amu is due to the additional length of higher (material A, 40 amu) or lower (material B, 120 amu) thermal conductivity material contributed by the interfacial film, whereas in the baseline case, equal amounts of both materials exist symmetrically about the interface (see Fig. 2).

Compared to the baseline h_{BD} value, varying degrees of enhancement are seen across all interfacial film thicknesses at 0.1 T_{m}. A maximum enhancement of approximately 23% is realized when the interfacial film mass approaches the average of the masses of material A and B. Moreover, the degree of enhancement exhibits a repeatable and symmetric dependence on the interfacial film mass (i.e., vibrational properties). The symmetric and inverse parabolic dependence on mass alludes to tunability. In so much as the vibrational properties of the interfacial film can be chosen, the enhanced structure can be tuned to exhibit certain degrees of enhancement.

There is only a weak dependence on the interfacial film thickness, which is attributed to the comparatively large MFP and resulting thermal conductivity of the three materials at 0.1 T_{m}. The relatively high thermal conductivity of material C requires a very thick interfacial film before the effects of diffusive thermal transport outweigh the benefits of the vibrational bridge and reduced temperature drop across the two interfaces.

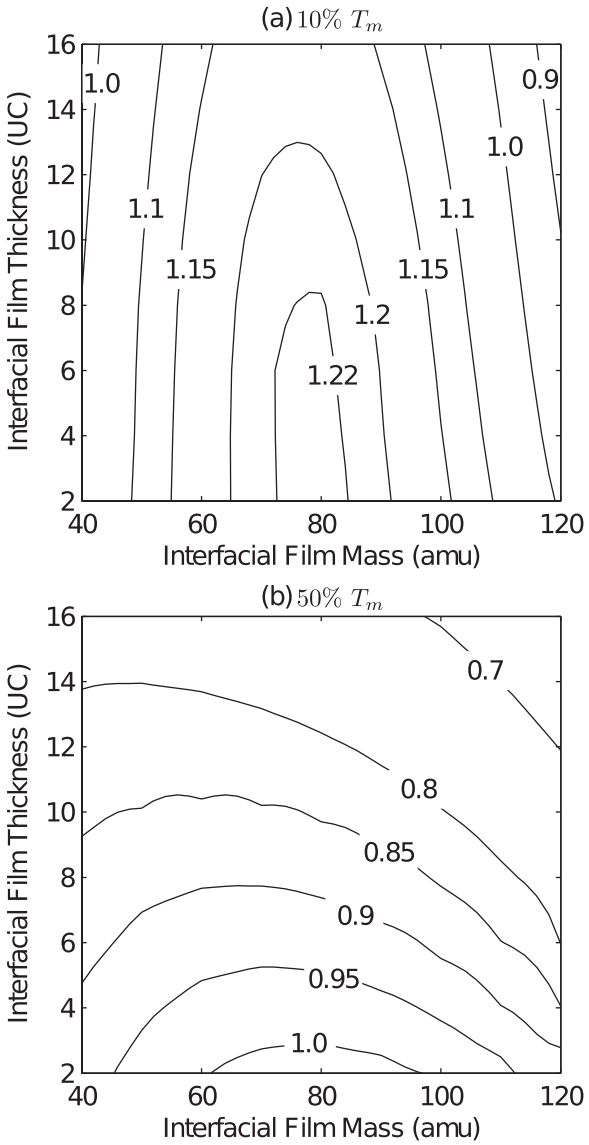

FIG. 7. Contour plot of h_{BD} values for varying interfacial film thickness and mass values. (a) Results of the 0.1 T_{m} study, which shows enhancement of h_{BD} of up to 23% and a nearly symmetric dependence on interfacial film mass. (b) Results of the 0.5 T_{m} study, for which enhancement of h_{BD} is found to be minimal and only for interfacial film thicknesses <4 UC.

B. High temperature (50% of melting temperature)

The results of the higher-temperature study are summarized in Fig. 7(b). In the case of the thinnest interfacial film (2 UC), the enhancement of h_{BD} is minimal (<5% at best). The reduction in h_{BD} with increasing interfacial film thickness indicates the dominance of diffusive thermal transport in the interfacial film and reduction in the phonon MFP at higher temperatures. It is apparent that the reduction in thermal

conductivity and phonon MFP limit the benefits offered by the vibrational bridge in the form of the interfacial film.

As shown in Fig. 3(c), thermal conductivity of the simulated materials is nearly an order of magnitude lower at 0.5 T_m than at 0.1 T_m, which corresponds to a nearly equal reduction in the phonon MFP. Using kinetic gas theory, thermal conductivity can be expressed as

$$k = \tfrac{1}{3} c_v v l, \tag{7}$$

where c_v is volumetric heat capacity, v is the phonon group velocity, and l is the phonon MFP. The reduction in k and associated change in MFP can be better understood by examining each component in Eq. (7).

In a classical and harmonic system, the kinetic and potential energies associated with each degree of freedom are making the same contribution of $1/2\,k_B$ to the heat capacity of the system. Therefore, in a three-dimensional system, $c_v = 3Nk_B\rho$, where N is Avagadro's number and ρ is molar density. The equipartition between kinetic and potential energies is not exact for systems described by anharmonic interatomic potentials and the deviation from the harmonic approximation is increasing with increasing temperature. However, the anharmonic effects on heat capacity are generally small,[41] and decrease the heat capacity only minimally with increasing temperature in fcc LJ crystals. MD studies have showed that c_v at 50% of the melt temperature is $\approx 95\%$ of the classical and harmonic prediction.[42] Therefore, at 0.5 T_m, the heat capacity cannot account for the large change in k. Similarly, any change in group velocity would be evident in the fully anharmonic dispersion relation calculated directly from the MD simulations[43,44] and shown in Fig. 8 along with the harmonic dispersion relation[25] for comparison. The primary anharmonic effect is a reduction (scaling) of the dispersion curves while the curvature remains almost the same. Because phonon group velocity is derived from the slope of the dispersion curves, anharmonicity has a negligible impact on phonon group velocity.

Finally, the half an order of magnitude reduction in k can be attributed directly to the reduction in the phonon MFP. The shorter MFP indicates a drastic increase in phonon-phonon scattering rates, which indicates that phonon thermal transport becomes limited due to the shorter intrinsic MFP. Any enhancement from mediating vibrational properties of an interfacial film at 0.5 T_m are outweighed by the increased frequency of Umklapp phonon-phonon scattering.

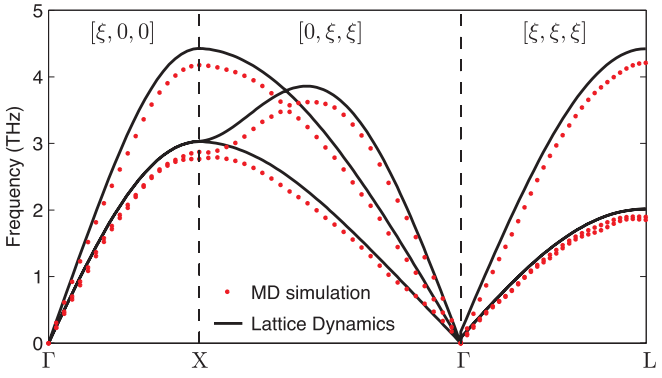

FIG. 8. (Color online) The phonon dispersion is shown for several directions of major symmetry. The solid lines show analytical calculations from harmonic lattice dynamics. The points are the anharmonic dispersion relationships from an MD simulation consisting of 512 atoms at 0.5 T_m and zero pressure.

It is worthwhile to summarize the implications of the enhancement of h_{BD} in this parametric study. The ability to enhance h_{BD} indicates that for a fixed heat flux and length of materials A and B along the direction of applied heat flux, the temperature drop across a lengthier sandwich structure of materials A and B with an interfacial film in between can be lower. This salient result implies, in contrast to macroscopic thermal transport theory, that the addition of more material forming a vibrational bridge can reduce thermal resistance associated with an interface.

C. Phonon properties of enhanced interface structures

The substantial enhancement of h_{BD} shown at 0.1 T_m may be better understood by examining the occupied phonon DOS measured directly from the MD simulations. Figure 9(a) shows the bulk occupied DOS for material A and B at 0.1 T_m along with the overlap between them. Subsequently, the DOS is independently resolved in the x, y, and z directions for the 72 atoms of material A and B, which reside in the monolayers on either side of the baseline interface. In comparison to the bulk-occupied DOS, this resolution of directionally dependent and local occupied DOS demonstrates that the phonon properties are perturbed in the monolayers near the interface. In Fig. 9(b), only the occupied DOS in the z direction is shown for clarity. The DOS in these monolayers show a massive redistribution of modes due to the presence of the interface and interactions beyond first-nearest-neighbor (NN) atoms including those residing in the adjacent (dissimilar) material. The redistribution of phonon modes in the monolayers adjacent to the interface is evidence of the existence of an interfacial transition layer. Such a layer has been shown to perturb the local vibrational properties adjacent to an interface, giving rise to intrinsic resonant modes[45] and enhanced phonon transmission.[46,47] This results in a DOS overlap at the interface spanning a much larger range of frequencies than is predicted using bulk phonon properties. Similar restructuring of phonon properties near an interface and the impact on h_{BD} have been shown in MD studies of solid-liquid interfaces.[48]

Due to the confined nature of the thinnest interfacial films, as well as the perturbation to phonon properties near each interface, the wave nature of phonons becomes important to consider. Coherent effects and phonon interference arising from these mechanisms are difficult to quantitatively assess using an *a priori* analytical expression. Instead, we examine the occupied, directionally dependent, and monolayer-resolved DOS for the enhanced interface structures to gain insight into the phonon properties at the interface that give rise to the enhancement of h_{BD}.

For example, enhancement of h_{BD} in the presence of the interfacial film can be understood by examining the spatially resolved DOS in the monolayers adjacent to the A:C interface for the most enhancing structure (8 UC thick, 80 amu interfacial film) at 0.1 T_m. The DOS in the z direction adjacent to both the A:B (baseline) and A:C interfaces are plotted in

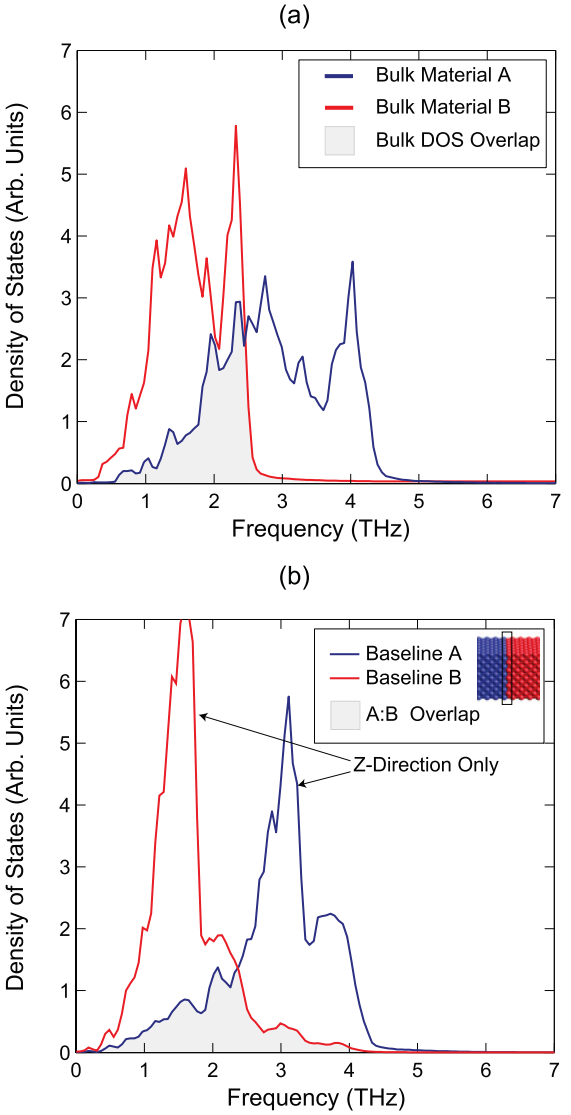

FIG. 9. (Color online) (a) Bulk and isotropic occupied DOS for material A (40 amu) and material B (120 amu). The shaded region outlines the overlap between the bulk DOS. (b) Occupied DOS along the z axis calculated from monolayers containing 72 atoms of material A and B, which reside on either side of the sharp baseline interface.

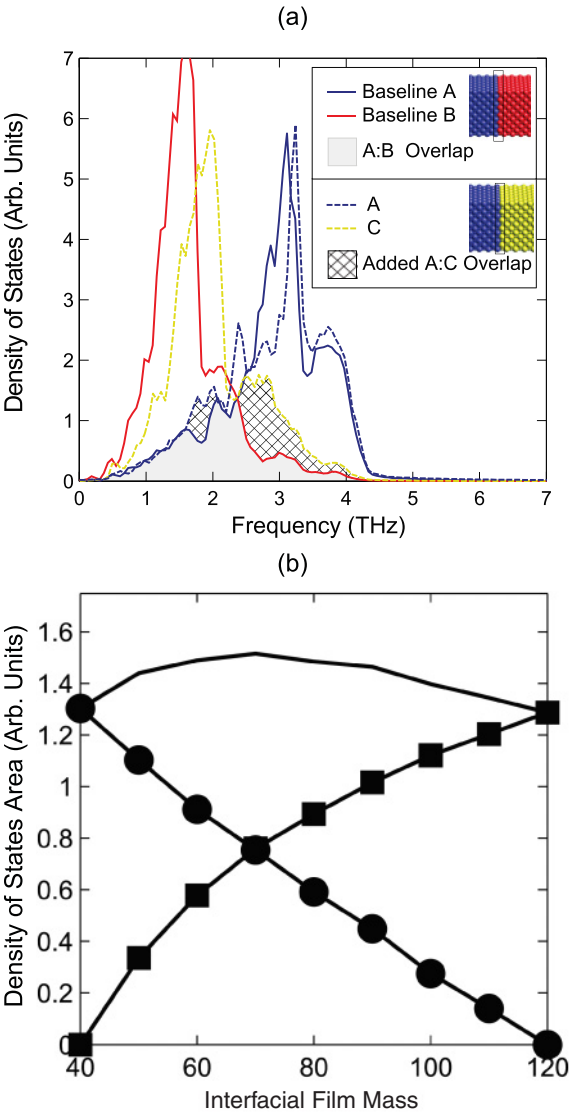

FIG. 10. (Color online) (a) DOS along the z axis calculated from monolayers containing 72 atoms of material A and C in the enhanced (8 UC, 80 amu) interface (dashed lines) in comparison to the baseline interface. The added overlap in the DOS is shown by the hatched region. (b) Integrated difference in the DOS area at each of the A:C and C:B interfaces for the 8-UC thickness interfacial film and varying mass values. The metric displays the tradeoffs in spreading the vibrational mismatch, which formerly occurs at a single interface, between the two new interfaces. An optimal value of the interfacial mass (80 amu) is observed, reflecting a maximum in the combined DOS overlap of both interfaces.

Fig. 10(a). The added overlap in DOS at the A:C interface is shown as a hatched region. The added overlap (increased density) of phonon modes between 1.5 and 4 THz increases elastic scattering channels and therefore phonon transmission at the interface.

In the context of thermal transport, this alteration to DOS, especially along the direction of thermal flux, lends insight into the enhancement of h_{BD} achieved with an interfacial film. The perturbation to the local DOS can be optimized to spread the difference in vibrational properties, which formerly occurred at a single interface (plane), across a few monolayers near the interface, over which phonon DOS and dispersion are perturbed. For phonons to scatter, they must coincide in both space and time. By inserting an interfacial film with mediating vibrational properties, this spatial constraint is relaxed and phonons have added volume (two interfaces) over which frequency up- or down-conversion may occur. A functionally graded phonon DOS is therefore created across the interfacial region by adding an interfacial film, which is better vibrationally matched to materials A and B than materials A and B are to one another.

To quantitatively assess the degree of overlap and conditions for optimal enhancement, we calculate the absolute value of the difference in DOS of the monolayers adjacent to each interface (A:C and C:B), and integrate the resulting area

$$\text{DOS Overlap Area}_{x,y} = \int |\text{DOS}_{\text{x}}(\omega) - \text{DOS}_{\text{y}}(\omega)|\, d\omega. \quad (8)$$

This metric is shown for the 8 UC thick, 80 amu, interfacial film at 0.1 T_m in Fig. 10(b). In the case of a 40 amu interfacial film mass, the A:C interface is nearly perfectly matched, with the direct result that the C:B interface exhibits a maximum vibrational mismatch. The converse is true in the case of the 120-amu interfacial film mass. By assessing the sum of the integrated area associated with both the A:C and C:B interface, a trade-off is found where the vibrational mismatch is optimally distributed between the two interfaces. The inverse parabolic trend of the total area curve in Fig. 10(b) closely resembles the functional dependence of h_{BD} on interfacial mass, as shown in Fig. 7(a). This provides further evidence that the functionally graded phonon DOS in the interfacial film can be optimized to bridge the mismatch in phonon properties at the baseline interface.

V. ENHANCEMENT AT COMPOSITIONALLY DISORDERED INTERFACES

Having investigated sharp interfaces, we also consider whether or not similar enhancement of h_{BD} can be realized at nonideal interfaces characterized by compositional disorder. To evaluate the role of compositional disorder at interfaces, each of the sharp A:C and C:B interfaces in the domains were modified in the following manner. Atomic mixing was introduced by statistically describing the distribution of atom type over a finite distance ($\pm z$) from the location of each sharp interface (A:C and C:B). A series of bounded univariate probability distribution functions were used to model atomic mixing, which provide control over the spatial extent and composition gradient in the mixing layer. A log-ratio Laplace distribution was selected for this study because it provides a closed interval space that does not extend to $\pm\infty$. Additionally, the shape of this distribution function is characteristic of many composition profiles obtained for AES and XPS line scans across interfaces where h_{BD} has also been experimentally measured.[49]

To construct the distribution function, a log transformation is used to transform a domain variable y with unbounded limits ($-\infty < y < \infty$) to a new domain, x, bounded between lower and upper limits η_L and η_U ($\eta_L < x < \eta_U$), where

$$y = ln\left(\frac{x-\eta_L}{\eta_U - x}\right). \tag{9}$$

The new transformed variable serves as the input to the standard Laplace distribution function $H(x)$,[50,51]

$$H(x) = \begin{cases} \frac{1}{2}\exp\left(\frac{x-\beta}{\alpha}\right) & \text{if } x \leqslant \beta, \\ 1 - \frac{1}{2}\exp\left(-\frac{x-\beta}{\alpha}\right) & \text{if } \beta \leqslant x, \end{cases} \tag{10}$$

where β is a location parameter ($-\infty < \beta < \infty$), and α is a scale parameter ($\alpha > 0$). Plots of the log-ratio Laplace distribution function for several values of α are shown in Fig. 11(a). The β parameter was set equal to zero throughout this study, which ensures that the distribution function evaluates to 0.5 at the midpoint of the mixing layer ($x = 0$ in Fig. 11(a)).

Atomic mixing at each interface was introduced using the distribution function to describe the probability that an atomic site is occupied by a particular atom type, with $\pm\eta$ equal to the number of unit cells perpendicular to the interface where the mixing layer was bounded. A schematic demonstrating the probability of each atom type across a compositionally disordered interfacial film structure is shown in Fig. 11(b). Three nonideal interface structures were studied, which are referenced with regard to their degree of compositional disorder as low, medium, and high. The constructed computational domains are shown in Fig. 12 for two different interfacial film thicknesses. The corresponding parameters and metrics of disorder are provided in Table II for each structure. The percent misplaced atoms quantifies the number of "wrong" atoms on atomic sites with respect to the sharp structures in the volume extending $\pm\eta$ UC from the A:C and C:B interfaces.

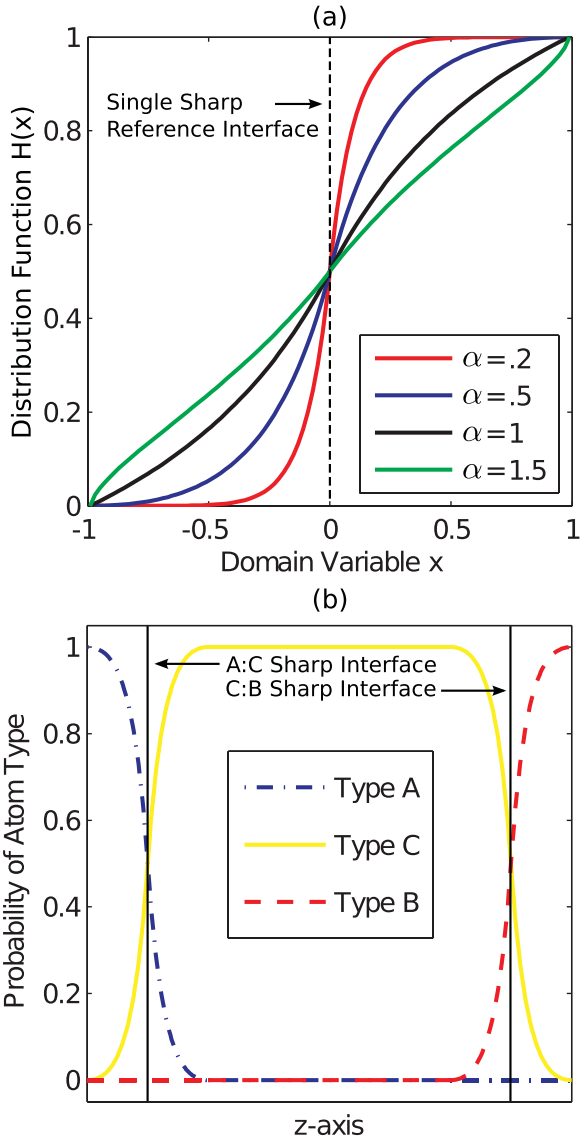

FIG. 11. (Color online) (a) Plot of the log-ratio Laplace distribution function for various values of α with $\eta_L = -1$ and $\eta_U = 1$. Compared to the step function associated with the sharp reference interface, the distribution function is capable of modeling more gradual transitions. (b) Schematic demonstrating the probability of atom type across the interfacial film region. Two distinct mixing regions are shown centered around the location of the A:C and C:B interfaces in the comparable sharp interface structures.

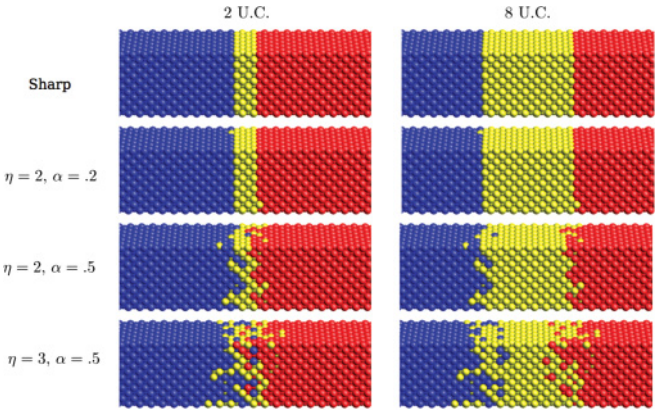

FIG. 12. (Color online) Computational domains showing the low, medium, and high levels of disorder for both the 2- and 8-UC-thick interfacial films in comparison to the sharp interface structure.

To ensure that each interface structure was evaluated in a self-consistent manner, the same arrangement of atoms in the compositionally disordered regions was used for varying thicknesses of the interfacial film for a given degree of order. The parametric study described previously was repeated for these compositionally disordered domains, and three independent simulations were performed across the parametric study to assess the repeatability of results.

A. Low temperature (10% of melt temperature)

Results at 0.1 T_m show a stronger degree of h_{BD} enhancement in both the low and medium disorder cases in comparison to the sharp interface results in Sec. IV. The greatest degree of enhancement is found in the medium disorder case which approaches 53% for the 2-UC-thick interfacial film over the baseline interface, which is an additional 30% improvement over the comparable sharp interface. The 4- and 6-UC interfacial films show similar enhancement of ~50% in the case of an 80 amu film mass. These results are summarized in Fig. 13 for the case of a 6-UC-thick interfacial film. The results for other film thicknesses are tabulated in Table III in the Appendix.

The highly disordered interface does not improve upon its sharp counterpart, but does not reduce h_{BD} significantly either. In comparison to these less aggressive levels of disorder, the high-disorder case creates a more abrupt transition in atomic composition, which has been shown experimentally to result in comparatively lower h_{BD} values.[49] Accordingly, this abrupt transition region more heavily scatters phonons near the boundary of the compositionally disordered region.

These results may be interpreted by considering the difference in phonon scattering between the sharp and compositionally disordered interfaces. In the case of an ideal, sharp, and vibrationally mismatched interface, phonons that exist above the lower cutoff frequency of the two materials, if they are to propagate across the interface, must scatter across the interface plane. Conversely, a mixing region provides an added volume for phonon frequency up- or down-conversion in which phonons scatter during diffusive thermal transport, and in doing so, access intermediary vibrational frequencies, which bridge the phonon DOS of the two materials comprising the interface. This phenomena is shown in Fig. 14, which plots the monolayer-resolved occupied DOS in the z direction for a medium-disordered A:C interface. Compared to the baseline interface, the medium level of disorder adds substantially to the overlap in DOS as shown by the hatched region. It is apparent that at 0.1 T_m, while disorder may improve the enhancement, the spatial extent and severity of compositional disorder determines the ultimate change in h_{BD}. Therefore we conclude that the presence of compositional disorder at an interface does not imply a deterministic change in h_{BD}, and that the specific characteristics of the disordered regions determine any impact on h_{BD}.

TABLE II. Compositional disorder modeling parameters.

Disorder	α	η (UC)	Percent misplaced atoms
low	0.2	2	0.8%
medium	0.5	2	5.5%
high	0.5	3	9.3%

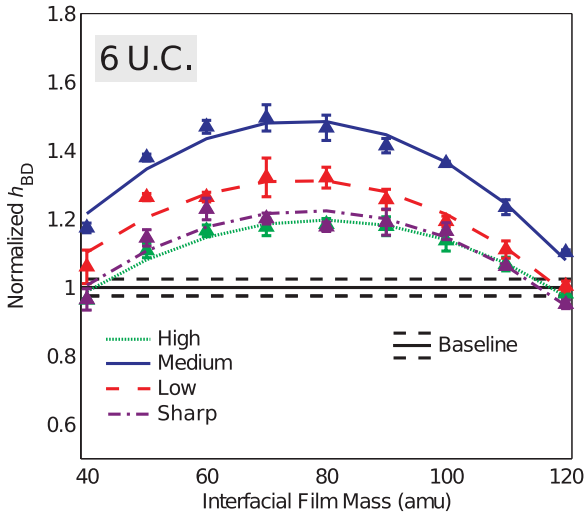

FIG. 13. (Color online) Interface conductance values as a function of interfacial film mass for the three disordered interfaces are plotted along with the comparable sharp interface at 0.1 T_m. Error bars represent one standard deviation of three independent simulations.

B. High temperature (50% of melting temperature)

At 0.5 T_m, the interfacial film tends to produce a reduction in h_{BD}. The general reduction in h_{BD} is attributed to the reduction in k and the phonon MFP as was discussed in Sec. IV B for the case of the sharp interface at 0.5 T_m. The mixing layer with bridging vibrational properties cannot be utilized as efficiently because the limiting factor, as in the case of the sharp film at 0.5 T_m, becomes the shorter intrinsic MFP and limited thermal conductivity. Additionally, preliminary simulations of the low-disorder case produced h_{BD} values, which were statistically indistinguishable from the sharp counterpart due to larger uncertainties at higher temperatures. As a result, no further simulations of the low-disorder case at 0.5 T_m were completed. The results of the 0.5 T_m study are tabulated in Table IV in the Appendix.

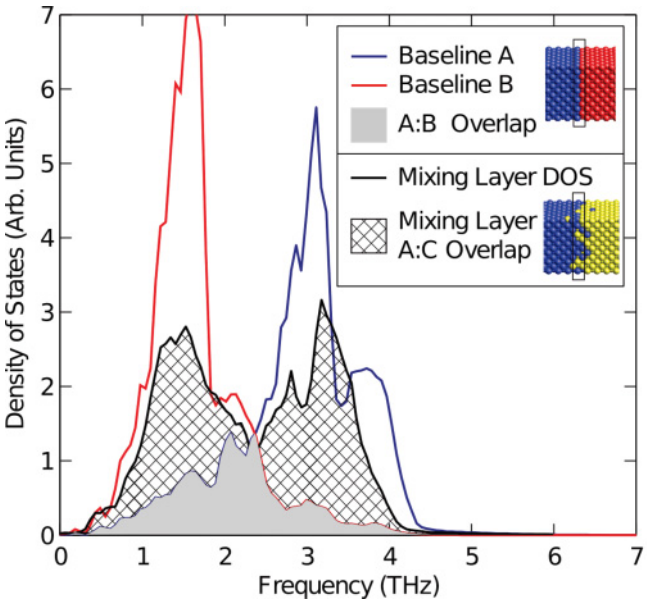

FIG. 14. (Color online) Comparison of the monolayer-resolved DOS along the z axis at the sharp A:B interface with the DOS in a monolayer of the mixing region for a medium-disordered interface with an interfacial atomic mass equal to 80 amu. The DOS in the disordered monolayer spans a much wider range of frequencies up to nearly the cutoff frequency in bulk material B.

VI. SUMMARY

In this manuscript, we investigate a method by which h_{BD} may be broadly enhanced and potentially tuned at vibrationally mismatched solid-solid interfaces. A parametric study is performed to provide a holistic description of the enhancing phenomena. The study explores the impact on h_{BD} of four parameters, including (1) temperature, (2) the vibrational spectrum of the interfacial film, (3) the thickness of the interfacial film, and (4) compositional disorder in the interfacial region.

(1) Both the sharp and compositionally disordered interface results exhibit a strong dependence on temperature. As shown in Fig. 3, between 0.1 and 0.5 T_m, the thermal conductivity of materials A and B lie in the regime where Umklapp phonon-phonon scattering dominates. Between 0.1 and 0.5 T_m, there is a transition from a large degree of enhancement shown at lower temperatures, to progressively lower enhancement, which scales with the reduction in MFP at higher temperatures. This transition is due to the effective thermal conductance across a multiple interface structure depending on both interface conductance and thermal conductivity in the region between interfaces. With increasing temperature, the reduction in k by nearly half an order of magnitude significantly limits any enhancement offered by the interfacial film.

(2) In nearly all simulations demonstrating enhancement, h_{BD} exhibits an inverse parabolic dependence on interfacial film mass. The vibrational properties of the interfacial film are optimized for enhancement of h_{BD} when the atomic mass of the interfacial film is nearly the average of the masses of the materials comprising the baseline interface, a condition similar to Debye temperature matching.[21]

(3) The dependence of h_{BD} on interfacial film thickness is strongest when the thermal conductivity of the interfacial film is comparatively low (i.e., at high temperature), which causes a rapid reduction in enhancement with increasing interfacial film thickness. Because temperature-dependent thermal conductivity and phonon MFP determine the maximum thickness where enhancement is observed, it is likely that an interface designed to enhance h_{BD} at a set temperature could perform worse than the baseline interface if operated at an off-design temperature. The maximum enhancement at sharp interfaces lies in between the thinnest film, which is extremely confined, and the thick films, where the added thermal resistance associated with diffusive thermal transport through the interfacial film outweighs the enhancement provided by the vibrational bridge. However, when considering interface disorder, maximum enhancement tended to exist at thinner interfacial film thicknesses.

(4) We find that compositional disorder at an interface does not imply a deterministic change in h_{BD}, as has been alluded to in previous studies. Instead, a lower level of detail prescribes whether enhancement to h_{BD} is observed, including the thickness of the mixing layer associated with disorder, as well as the sharpness of the composition profile across the mixing layer. We observe that increasing the volume of the mixing region eventually causes reduction in h_{BD}. Compositional disorder at 50% of the melting temperature is shown to strongly reduce h_{BD} at higher temperatures. As has been shown in previous studies, however, at low temperature, disorder can strongly enhance h_{BD}.[52] At these temperatures, the sharpness of the change in atomic composition at an interface is also shown to strongly influence h_{BD}. We find that a more gradual spatial change in composition at an interface results in greater h_{BD} enhancement.

Our results suggest that while increased DOS overlap at an interface is generally associated with increased h_{BD}, the presence of a compositionally disordered mixing region impacts the relationship between DOS overlap and h_{BD}. Therefore disorder can lead to either enhancement or reduction in h_{BD}. For sharp interfaces, important modifications to vibrational properties and phonon scattering associated with the presence of an interface are localized to the monolayers adjacent to the interface. Subsequent to scattering at an interface, phonons are more likely to travel away from the perturbed interface region before scattering again. In this case, we observe a direct increase in h_{BD} with an increase in DOS overlap due to increased elastic scattering channels at the interface. This relationship is evident when comparing the similar inverse parabolic dependence of the overlap in DOS on interfacial film mass in Fig. 10(b) with the inverse parabolic dependence of h_{BD} on interfacial film mass in Fig. 7. The interfacial film mass for which the maximum increase in h_{BD} is observed is the same value (70 to 80 amu) where the maximum overlap in DOS is observed. Furthermore, for the compositionally sharp interfacial film in Fig. 4(b), the temperature drop at each interface is well defined, suggesting that the effects of interface scattering are localized at the abrupt temperature drop.

However, in the case of compositional disorder, modifications to phonon scattering associated with the presence of an interface are no longer localized to a plane at the interface, but extend over a volume dependent upon the spatial extent of the mixing region. This is clearly seen in the temperature profile of the medium disorder interfacial film in Fig. 4(c) where

abrupt temperature drops are not observed. Additionally, in the 0.1 T_m study of the high-disorder interfacial film, although a significant DOS overlap increase was found within the mixing region similar to that in the medium- and low-disorder cases, no corresponding increase in h_{BD} was observed. This suggests that the MFPs of the dominant phonons contributing to thermal transport are important in determining the spatial extent and severity of disorder, which lead to either enhancement or reduction in h_{BD}.

In conclusion, an interfacial film with mediating vibrational properties may enhance h_{BD} by up to 23% in ideal (sharp) interface structures and 53% in nonideal (compositionally disordered) interfaces. As discussed, the temperature, MFP, and phonon DOS in the vicinity of an interface are important factors in the enhancing phenomena. Therefore we expect the degree of enhancement to be dependent on both the materials comprising the interfaces as well as interface bonding,[53] where materials with a larger intrinsic phonon MFP can be expected to exhibit even greater degrees of enhancement than those reported here for fcc LJ solids. In cases where h_{BD} is the dominant factor limiting total conductance, we find that, in contrast to macroscopic thermal transport theory, the temperature drop across a lengthier interface structure can in fact be smaller. This implies that additional material forming an interfacial film can reduce the thermal resistance associated with an interface.

ACKNOWLEDGMENTS

The authors would like to acknowledge financial support from the Air Force Office of Scientific Research (Grant No. FA9550-09-1-0245) as well as the other members of the U.Va. Nanoscale Energy Transport Laboratory for insightful feedback on this research. T.S.E. and J.C.D. are grateful for financial support from the National Science Foundation through the Graduate Research Fellowship Program, and L.V.Z. acknowledges support from the National Science Foundation (CBET-1033919).

APPENDIX: SUMMARY OF MD SIMULATION RESULTS

TABLE III. Interface conductance values tabulated for the 0.1 T_m study, where h_{BD} values are the average of five independent simulations. The associated standard deviations are reported. For each mass value, an individual row presents the sharp (E), low- (L), medium- (M), and high- (H) disorder results.

		Interfacial film thickness (UC)															
		0.1 T_m															
		2		4		6		8		10		12		14		16	
Mass (amu)		h_{BD}	std	h_{BD}	std	h_{BD}	std	h_{BD}	std	h_{BD}	std	h_{BD}	std	h_{BD}	std	h_{BD}	std
40	E	0.988	1.5×10^{-2}	0.976	1.7×10^{-2}	0.967	2.2×10^{-2}	0.961	5.5×10^{-3}	0.963	1.9×10^{-2}	0.945	8.0×10^{-3}	0.939	1.2×10^{-2}	0.937	1.3×10^{-2}
	L	1.063	1.2×10^{-2}	1.060	2.7×10^{-2}	1.036	1.2×10^{-2}	1.027	1.2×10^{-2}	1.031	2.4×10^{-2}	1.010	2.0×10^{-2}	1.018	1.4×10^{-2}	0.991	7.8×10^{-3}
	M	1.232	3.6×10^{-2}	1.200	1.9×10^{-2}	1.167	5.4×10^{-3}	1.164	1.2×10^{-2}	1.112	2.0×10^{-2}	1.141	2.6×10^{-2}	1.116	3.0×10^{-2}	1.095	3.5×10^{-2}
	H	1.018	2.9×10^{-2}	1.002	6.5×10^{-4}	0.963	4.4×10^{-3}	0.972	3.0×10^{-2}	0.954	1.4×10^{-2}	0.954	1.7×10^{-2}	0.907	2.7×10^{-2}	0.911	5.0×10^{-3}
50	E	1.170	1.5×10^{-2}	1.160	3.1×10^{-2}	1.154	2.3×10^{-2}	1.168	1.8×10^{-2}	1.140	1.8×10^{-2}	1.125	1.1×10^{-2}	1.122	4.2×10^{-2}	1.098	2.4×10^{-2}
	L	1.266	2.0×10^{-2}	1.242	3.0×10^{-2}	1.273	6.8×10^{-3}	1.249	3.6×10^{-2}	1.202	3.5×10^{-2}	1.230	2.3×10^{-2}	1.212	8.4×10^{-3}	1.182	2.6×10^{-2}
	M	1.415	1.2×10^{-2}	1.423	3.7×10^{-2}	1.398	1.1×10^{-2}	1.378	2.4×10^{-2}	1.373	1.8×10^{-2}	1.350	5.2×10^{-2}	1.323	1.0×10^{-3}	1.299	1.7×10^{-2}
	H	1.151	2.0×10^{-2}	1.101	1.8×10^{-2}	1.119	1.4×10^{-2}	1.082	3.7×10^{-3}	1.059	1.8×10^{-4}	1.064	2.7×10^{-2}	1.050	2.8×10^{-4}	1.039	4.8×10^{-3}
60	E	1.201	2.1×10^{-2}	1.175	1.8×10^{-2}	1.230	2.3×10^{-2}	1.194	2.3×10^{-2}	1.181	2.2×10^{-2}	1.178	1.9×10^{-2}	1.194	1.7×10^{-2}	1.153	2.4×10^{-2}
	L	1.328	4.1×10^{-2}	1.309	1.8×10^{-2}	1.263	1.6×10^{-2}	1.310	1.1×10^{-2}	1.274	7.2×10^{-3}	1.256	4.7×10^{-2}	1.255	2.3×10^{-2}	1.226	1.6×10^{-2}
	M	1.523	4.0×10^{-2}	1.450	2.9×10^{-3}	1.488	4.5×10^{-3}	1.415	6.5×10^{-3}	1.423	3.2×10^{-2}	1.406	1.8×10^{-2}	1.378	3.1×10^{-2}	1.343	1.5×10^{-2}
	H	1.171	5.5×10^{-3}	1.134	4.5×10^{-4}	1.157	9.2×10^{-3}	1.154	5.0×10^{-3}	1.100	2.3×10^{-2}	1.105	1.9×10^{-2}	1.111	1.3×10^{-2}	1.083	3.5×10^{-2}
70	E	1.185	8.3×10^{-3}	1.181	2.0×10^{-2}	1.205	1.7×10^{-2}	1.215	3.7×10^{-2}	1.195	2.4×10^{-2}	1.197	2.9×10^{-2}	1.171	1.1×10^{-2}	1.175	2.9×10^{-2}
	L	1.293	3.8×10^{-2}	1.308	2.1×10^{-2}	1.331	7.8×10^{-2}	1.339	4.3×10^{-2}	1.266	2.1×10^{-2}	1.283	5.2×10^{-3}	1.266	1.9×10^{-2}	1.256	1.4×10^{-2}
	M	1.526	1.3×10^{-2}	1.500	5.1×10^{-2}	1.497	5.7×10^{-2}	1.465	2.7×10^{-2}	1.437	4.3×10^{-2}	1.410	5.5×10^{-2}	1.389	1.5×10^{-2}	1.358	1.8×10^{-2}
	H	1.231	4.3×10^{-2}	1.175	3.4×10^{-2}	1.164	1.6×10^{-2}	1.160	1.5×10^{-2}	1.153	5.0×10^{-3}	1.137	9.6×10^{-3}	1.116	2.8×10^{-2}	1.095	1.3×10^{-2}
80	E	1.204	2.7×10^{-2}	1.198	2.3×10^{-2}	1.180	2.3×10^{-2}	1.228	2.4×10^{-2}	1.196	3.2×10^{-2}	1.194	1.5×10^{-2}	1.193	9.6×10^{-3}	1.168	2.2×10^{-2}
	L	1.290	1.1×10^{-2}	1.322	1.7×10^{-2}	1.332	3.9×10^{-2}	1.270	6.2×10^{-3}	1.270	9.1×10^{-3}	1.229	2.2×10^{-2}	1.221	2.3×10^{-2}	1.204	2.9×10^{-2}
	M	1.510	1.8×10^{-2}	1.459	1.1×10^{-2}	1.480	4.8×10^{-3}	1.446	3.9×10^{-2}	1.443	4.4×10^{-2}	1.395	1.4×10^{-2}	1.357	1.7×10^{-2}	1.326	5.4×10^{-2}
	H	1.230	3.4×10^{-3}	1.236	5.6×10^{-2}	1.189	2.2×10^{-2}	1.178	3.0×10^{-2}	1.168	6.2×10^{-3}	1.122	1.7×10^{-3}	1.123	1.7×10^{-2}	1.112	2.6×10^{-2}
90	E	1.199	3.4×10^{-2}	1.203	2.3×10^{-2}	1.184	2.9×10^{-2}	1.184	1.6×10^{-2}	1.165	2.3×10^{-2}	1.164	1.6×10^{-2}	1.140	2.0×10^{-2}	1.114	3.2×10^{-2}
	L	1.289	2.6×10^{-2}	1.264	3.6×10^{-2}	1.276	1.6×10^{-2}	1.297	3.4×10^{-2}	1.217	5.7×10^{-3}	1.251	6.3×10^{-3}	1.228	1.5×10^{-2}	1.178	1.0×10^{-2}
	M	1.483	1.7×10^{-2}	1.448	4.3×10^{-2}	1.394	1.9×10^{-4}	1.349	4.3×10^{-2}	1.355	2.7×10^{-2}	1.339	2.6×10^{-2}	1.280	2.4×10^{-2}	1.244	1.5×10^{-2}
	H	1.225	3.2×10^{-2}	1.174	2.4×10^{-2}	1.163	6.7×10^{-3}	1.138	5.7×10^{-5}	1.157	1.0×10^{-2}	1.124	1.8×10^{-2}	1.086	1.7×10^{-2}	1.088	1.0×10^{-2}
100	E	1.164	1.7×10^{-2}	1.160	8.6×10^{-3}	1.155	2.4×10^{-2}	1.141	2.2×10^{-2}	1.131	2.8×10^{-2}	1.119	2.3×10^{-2}	1.089	2.5×10^{-2}	1.075	1.3×10^{-2}
	L	1.271	2.5×10^{-2}	1.224	2.3×10^{-2}	1.188	7.5×10^{-3}	1.193	1.8×10^{-2}	1.175	3.7×10^{-2}	1.132	2.3×10^{-2}	1.152	1.4×10^{-2}	1.100	2.8×10^{-2}
	M	1.381	3.5×10^{-2}	1.369	1.9×10^{-2}	1.343	3.9×10^{-2}	1.296	2.2×10^{-2}	1.331	4.0×10^{-2}	1.232	1.5×10^{-2}	1.240	2.0×10^{-2}	1.206	1.6×10^{-2}
	H	1.154	6.7×10^{-3}	1.154	3.3×10^{-2}	1.145	3.9×10^{-2}	1.061	1.4×10^{-2}	1.101	2.9×10^{-2}	1.066	2.9×10^{-2}	1.051	9.1×10^{-3}	1.019	4.0×10^{-2}
110	E	1.110	6.5×10^{-3}	1.083	1.7×10^{-2}	1.056	1.8×10^{-2}	1.042	1.1×10^{-2}	1.041	5.1×10^{-3}	1.000	1.9×10^{-2}	1.000	2.1×10^{-2}	0.968	3.1×10^{-2}
	L	1.179	6.9×10^{-3}	1.127	2.3×10^{-2}	1.125	2.4×10^{-2}	1.082	6.3×10^{-3}	1.099	3.7×10^{-2}	1.064	1.2×10^{-2}	1.019	1.0×10^{-2}	1.008	1.8×10^{-2}
	M	1.311	3.3×10^{-2}	1.241	9.0×10^{-3}	1.220	1.4×10^{-2}	1.229	9.0×10^{-3}	1.184	1.9×10^{-2}	1.156	2.9×10^{-2}	1.128	2.6×10^{-2}	1.100	1.3×10^{-2}
	H	1.124	3.1×10^{-2}	1.107	7.8×10^{-3}	1.078	1.4×10^{-2}	1.082	2.9×10^{-2}	1.019	1.6×10^{-2}	0.997	6.5×10^{-3}	0.980	5.0×10^{-2}	0.960	5.0×10^{-3}
120	E	0.989	1.3×10^{-2}	0.944	1.8×10^{-2}	0.945	1.2×10^{-2}	0.926	3.0×10^{-2}	0.907	1.1×10^{-2}	0.892	1.3×10^{-2}	0.879	1.7×10^{-2}	0.855	5.8×10^{-3}
	L	1.044	1.1×10^{-2}	1.014	7.4×10^{-3}	1.005	2.0×10^{-2}	0.966	1.0×10^{-2}	0.954	1.2×10^{-2}	0.938	1.4×10^{-2}	0.901	2.2×10^{-2}	0.906	1.9×10^{-2}
	M	1.132	2.7×10^{-2}	1.131	5.9×10^{-3}	1.115	2.2×10^{-2}	1.076	1.6×10^{-2}	1.046	2.2×10^{-3}	1.027	8.6×10^{-3}	1.013	3.0×10^{-2}	1.011	1.3×10^{-2}
	H	1.017	2.9×10^{-3}	0.986	1.4×10^{-2}	0.972	5.6×10^{-3}	0.956	2.5×10^{-2}	0.949	2.7×10^{-2}	0.928	1.1×10^{-2}	0.906	1.2×10^{-2}	0.889	1.2×10^{-3}

TABLE IV. Interface conductance values tabulated for the 0.5 T_m study, where h_{BD} values are the average of three independent simulations. The associated standard deviations are reported. For each mass value, an individual row presents the sharp (E), medium- (M), and high- (H) disorder results.

			Interfacial film thickness (UC)															
			0.5 T_m															
			2		4		6		8		10		12		14		16	
			h_{BD}	std	h_{BD}	std	h_{BD}	std	h_{BD}	std	h_{BD}	std	h_{BD}	std	h_{BD}	std	h_{BD}	std
Mass (amu)	40	E	0.919	3.8×10^{-2}	0.890	1.9×10^{-2}	0.892	3.5×10^{-2}	0.855	3.2×10^{-2}	0.839	9.3×10^{-2}	0.807	8.5×10^{-2}	0.771	4.1×10^{-2}	0.786	4.8×10^{-2}
		M	1.003	2.9×10^{-2}	0.921	6.6×10^{-2}	0.952	3.5×10^{-2}	0.847	4.2×10^{-2}	0.849	4.1×10^{-2}	0.794	5.9×10^{-3}	0.843	1.5×10^{-2}	0.740	3.6×10^{-2}
		H	0.880	4.0×10^{-2}	0.758	5.4×10^{-2}	0.784	6.0×10^{-2}	0.804	3.2×10^{-2}	0.759	3.8×10^{-2}	0.716	1.2×10^{-2}	0.734	2.8×10^{-2}	0.711	7.3×10^{-2}
	50	E	0.965	7.8×10^{-2}	1.002	8.2×10^{-2}	0.880	8.9×10^{-2}	0.928	8.8×10^{-2}	0.821	4.0×10^{-2}	0.833	4.9×10^{-2}	0.846	3.4×10^{-2}	0.775	3.5×10^{-2}
		M	1.008	3.6×10^{-2}	0.920	3.7×10^{-2}	0.872	1.9×10^{-2}	0.872	8.5×10^{-2}	0.858	2.0×10^{-2}	0.835	2.4×10^{-2}	0.798	5.9×10^{-2}	0.718	7.4×10^{-2}
		H	0.930	6.6×10^{-2}	0.843	5.0×10^{-2}	0.837	3.7×10^{-2}	0.846	3.1×10^{-2}	0.810	5.8×10^{-2}	0.729	3.4×10^{-2}	0.684	2.8×10^{-2}	0.688	3.1×10^{-2}
	60	E	0.978	5.1×10^{-2}	0.945	7.4×10^{-2}	0.962	3.1×10^{-2}	0.890	6.4×10^{-2}	0.843	7.9×10^{-2}	0.808	5.4×10^{-2}	0.797	4.2×10^{-2}	0.745	2.4×10^{-2}
		M	0.991	8.5×10^{-2}	0.910	1.9×10^{-2}	0.900	9.9×10^{-2}	0.816	2.6×10^{-2}	0.820	4.7×10^{-2}	0.796	4.0×10^{-2}	0.790	1.9×10^{-2}	0.731	6.5×10^{-2}
		H	0.910	2.9×10^{-2}	0.853	1.1×10^{-1}	0.835	4.4×10^{-2}	0.801	3.6×10^{-2}	0.792	2.8×10^{-2}	0.780	3.0×10^{-2}	0.725	1.7×10^{-2}	0.719	4.8×10^{-2}
	70	E	1.022	1.5×10^{-1}	0.961	3.8×10^{-2}	0.922	7.2×10^{-2}	0.917	7.2×10^{-2}	0.868	5.0×10^{-2}	0.835	3.9×10^{-2}	0.798	7.1×10^{-2}	0.767	2.3×10^{-2}
		M	0.910	4.2×10^{-2}	0.930	7.8×10^{-2}	0.834	7.1×10^{-2}	0.863	1.4×10^{-1}	0.805	4.3×10^{-2}	0.771	1.2×10^{-2}	0.716	1.1×10^{-2}	0.732	3.2×10^{-2}
		H	0.949	3.9×10^{-2}	0.887	3.8×10^{-2}	0.803	5.6×10^{-2}	0.781	4.3×10^{-2}	0.726	4.5×10^{-2}	0.702	4.5×10^{-2}	0.696	2.7×10^{-2}	0.680	3.3×10^{-2}
	80	E	1.027	1.1×10^{-1}	0.978	7.4×10^{-2}	0.942	4.3×10^{-2}	0.892	3.5×10^{-2}	0.826	3.5×10^{-2}	0.802	3.1×10^{-2}	0.764	7.1×10^{-2}	0.721	3.5×10^{-2}
		M	0.916	4.9×10^{-2}	0.912	4.6×10^{-2}	0.889	4.4×10^{-2}	0.858	8.6×10^{-2}	0.818	3.9×10^{-2}	0.798	8.3×10^{-2}	0.742	3.8×10^{-2}	0.691	5.3×10^{-2}
		H	0.881	4.8×10^{-2}	0.877	6.3×10^{-2}	0.787	3.6×10^{-2}	0.779	6.4×10^{-2}	0.761	5.9×10^{-2}	0.702	5.5×10^{-2}	0.685	5.1×10^{-2}	0.627	2.0×10^{-2}
	90	E	1.041	1.0×10^{-1}	0.969	9.4×10^{-2}	0.863	5.5×10^{-2}	0.918	7.4×10^{-2}	0.800	2.1×10^{-2}	0.798	6.8×10^{-2}	0.750	4.0×10^{-2}	0.730	3.8×10^{-2}
		M	1.030	7.9×10^{-2}	0.906	2.6×10^{-2}	0.893	1.3×10^{-1}	0.813	7.0×10^{-2}	0.780	5.1×10^{-2}	0.791	3.2×10^{-2}	0.714	3.4×10^{-2}	0.704	4.4×10^{-3}
		H	0.879	3.8×10^{-2}	0.851	7.9×10^{-2}	0.807	3.4×10^{-2}	0.768	4.2×10^{-2}	0.754	2.5×10^{-2}	0.714	6.7×10^{-3}	0.727	2.9×10^{-2}	0.664	1.8×10^{-2}
	100	E	1.002	3.2×10^{-2}	0.956	1.1×10^{-1}	0.892	3.3×10^{-2}	0.780	5.6×10^{-2}	0.826	2.1×10^{-2}	0.769	5.8×10^{-2}	0.709	4.4×10^{-2}	0.711	4.8×10^{-2}
		M	0.950	8.3×10^{-2}	0.920	7.5×10^{-2}	0.807	5.0×10^{-2}	0.830	3.1×10^{-2}	0.802	1.0×10^{-2}	0.721	1.7×10^{-2}	0.706	4.5×10^{-2}	0.673	5.7×10^{-3}
		H	0.862	5.2×10^{-2}	0.898	4.0×10^{-2}	0.806	7.2×10^{-2}	0.762	4.4×10^{-2}	0.750	5.2×10^{-2}	0.661	5.1×10^{-2}	0.683	5.0×10^{-2}	0.650	4.3×10^{-2}
	110	E	0.925	4.7×10^{-2}	0.881	4.8×10^{-2}	0.861	7.5×10^{-2}	0.796	4.8×10^{-2}	0.739	4.4×10^{-2}	0.723	4.4×10^{-2}	0.705	1.9×10^{-2}	0.666	4.2×10^{-2}
		M	1.033	5.8×10^{-2}	0.897	4.3×10^{-2}	0.906	6.0×10^{-2}	0.887	3.8×10^{-2}	0.778	4.2×10^{-2}	0.721	2.0×10^{-2}	0.679	7.1×10^{-3}	0.689	5.2×10^{-2}
		H	0.859	5.0×10^{-2}	0.812	8.1×10^{-2}	0.813	6.0×10^{-2}	0.744	2.0×10^{-2}	0.708	3.8×10^{-2}	0.700	5.3×10^{-2}	0.683	5.9×10^{-2}	0.627	6.0×10^{-2}
	120	E	0.988	5.3×10^{-2}	0.820	5.2×10^{-2}	0.784	5.0×10^{-2}	0.805	3.8×10^{-2}	0.749	5.3×10^{-2}	0.711	3.7×10^{-2}	0.658	2.4×10^{-2}	0.645	4.9×10^{-2}
		M	0.911	3.4×10^{-2}	0.877	7.4×10^{-2}	0.849	4.0×10^{-2}	0.760	5.0×10^{-2}	0.770	4.0×10^{-2}	0.724	1.7×10^{-2}	0.713	2.8×10^{-2}	0.680	1.4×10^{-2}
		H	0.868	4.4×10^{-2}	0.759	4.2×10^{-2}	0.774	4.2×10^{-2}	0.733	5.2×10^{-2}	0.659	2.5×10^{-2}	0.660	2.3×10^{-2}	0.664	5.4×10^{-2}	0.638	2.3×10^{-2}

*tse8v@virginia.edu
†pamela@virginia.edu
‡lz2n@virginia.edu

[1] E. T. Swartz and R. O. Pohl, Rev. Mod. Phys. **61**, 605 (1989).
[2] D. G. Cahill, W. K. Ford, K. E. Goodson, G. D. Mahan, A. Majumdar, H. J. Maris, R. Merlin, and S. R. Phillpot, J. Appl. Phys. **93**, 793 (2003).
[3] G. Chen, J. Heat Transfer **119**, 220 (1997).
[4] C. Dames and G. Chen, J. Appl. Phys. **95**, 682 (2004).
[5] S. P. Hepplestone and G. P. Srivastava, J. Appl. Phys. **107**, 043504 (2010).
[6] G. Scamarcio, M. S. Vitiello, V. Spagnolo, S. Kumar, B. Williams, and Q. Hu, Physica E: Low-dimensional Systems and Nanostructures **40**, 1780 (2008), 13th International Conference on Modulated Semiconductor Structures.
[7] A. Lops, V. Spagnolo, and G. Scamarcio, J. Appl. Phys. **100**, 043109 (2006).
[8] K. P. Ghatak, S. Bhattacharya, D. De, K. P. Ghatak, S. Bhattacharya, and D. De, *Photoemission from Optoelectronic Materials and their Nanostructures*, Nanostructure Science and Technology, edited by D. J. Lockwood (Springer, New York, 2009), pp. 173–217.
[9] W. S. Capinski, H. J. Maris, T. Ruf, M. Cardona, K. Ploog, and D. S. Katzer, Phys. Rev. B **59**, 8105 (1999).
[10] K. E. Goodson and Y. S. Ju, Annu. Rev. Mater. Sci. **29**, 261 (1999).
[11] R. Prasher, Proceedings of the IEEE **94**, 1571 (2006).
[12] S. B. Riffat and X. Ma, Appl. Therm. Eng. **23**, 913 (2003).
[13] J. P. Reifenberg, D. L. Kencke, and K. E. Goodson, IEEE Electr. Device Lett. **29**, 1112 (2008).
[14] J. P. Reifenberg, K. Chang, M. A. Panzer, S. Kim, J. A. Rowlette, M. Asheghi, H.-S. P. Wong, and K. E. Goodson, IEEE Electr. Device Lett. **31**, 56 (2010).
[15] P. E. Phelan, J. Heat Transf. **120**, 37 (1998).
[16] E. Pop, Nano Res. **3**, 147 (2010).
[17] W. Kim, R. Wang, and A. Majumdar, Nanotoday **2**, 40 (2007).
[18] P. K. Schelling, S. R. Phillpot, and P. Keblinski, Appl. Phys. Lett. **80**, 2484 (2002).
[19] P. K. Schelling and P. Keblinski, Phys. Rev. B **68**, 035425 (2003).
[20] A. J. H. McGaughey, M. I. Hussein, E. S. Landry, M. Kaviany, and G. M. Hulbert, Phys. Rev. B **74**, 104304 (2006).
[21] R. J. Stevens, L. V. Zhigilei, and P. M. Norris, Int. J. Heat Mass Transf. **50**, 3977 (2007).
[22] J. W. Lyver IV and E. Blaisten-Barojas, J. Phys. Condens. Matter **21**, 345402 (2009).
[23] S. Ju, X. Liang, and S. Wang, J. Phys. D: Appl. Phys. **43**, 085407 (2010).
[24] A. Skye and P. K. Schelling, J. Appl. Phys. **103**, 113524 (2008).
[25] J. D. Gale and A. L. Rohl, Mol. Simul. **29**, 291 (2003).
[26] W. A. Little, Can. J. Phys. **37**, 334 (1959).
[27] D. A. Young and H. J. Maris, Phys. Rev. B **40**, 3685 (1989).
[28] G. Chen, Phys. Rev. B **57**, 14958 (1998).
[29] E. S. Landry, M. I. Hussein, and A. J. H. McGaughey, Phys. Rev. B **77**, 184302 (2008).
[30] N. A. Roberts, D. G. Walker, and D. Y. Li, Int. J. Heat Mass Transf. **52**, 2002 (2009).
[31] K. Termentzidis, P. Chantrenne, and P. Keblinski, Phys. Rev. B **79**, 214307 (2009).

[32]C.-J. Twu and J.-R. Ho, Phys. Rev. B **67**, 205422 (2003).
[33]T. S. English, J. C. Duda, D. A. Jordan, P. M. Norris, and L. V. Zhigilei, ASME Conf. Proc. **6**, 443 (2010).
[34]N. A. Roberts and D. G. Walker, J. Appl. Phys. **108**, 123515 (2010).
[35]K. V. Tretiakov and S. Scandolo, J. Chem. Phys. **120**, 3765 (2004).
[36]S. D. Stoddard and J. Ford, Phys. Rev. A **8**, 1504 (1973).
[37]H. J. C. Berendsen, J. P. M. Postma, W. F. van Gunsteren, A. DiNola, and J. R. Haak, J. Chem. Phys. **81**, 3684 (1984).
[38]D. S. Ivanov and L. V. Zhigilei, Phys. Rev. B **68**, 064114 (2003).
[39]D. P. Sellan, E. S. Landry, J. E. Turney, A. J. H. McGaughey, and C. H. Amon, Phys. Rev. B **81**, 214305 (2010).
[40] F. J. Harris, Proceedings of the IEEE **66**, 51 (1978).
[41]M. T. Dove, *Introduction to Lattice Dynamics* (Cambridge University Press, Cambridge, UK, 1993).
[42]A. J. H. McGaughey and M. Kaviany, Int. J. Heat Mass Transf. **47**, 1799 (2004).
[43]L. T. Kong, Comput. Phys. Commun. **182**, 2201 (2011).
[44]S. Plimpton, J. Comput. Phys. **117**, 1 (1995).
[45]C. F. Carlborg, J. Shiomi, and S. Maruyama, Phys. Rev. B **78**, 205406 (2008).
[46]L. Challis, J. Phys. C **7**, 481 (1974).
[47]Y. A. Kosevich, Phys. Rev. B **52**, 1017 (1995).
[48]S. Shin, M. Kaviany, T. Desai, and R. Bonner, Phys. Rev. B **82**, 081302 (2010).
[49]P. E. Hopkins, P. M. Norris, R. J. Stevens, T. E. Beechem, and S. Graham, J. Heat Transf. **130**, 062402 (2008).
[50]N. L. Johnson, S. Kotz, and N. Balakrishnan, *Continuous Univariate Distributions* (Wiley, New York, 1994), Vol. 1.
[51]N. L. Johnson, S. Kotz, and N. Balakrishnan, *Continuous Univariate Distributions* (Wiley, New York, 1995), Vol. 2.
[52]D. Kechrakos, J. Phys. Condens. Matter **3**, 1443 (1991).
[53]J. C. Duda, T. S. English, E. S. Piekos, W. A. Soffa, L. V. Zhigilei, and P. E. Hopkins, Phys. Rev. B **84**, 193301 (2011).